Article:

Wood, AM, Paton, DA and Collier, REL (2015) The missing complexity in seismically imaged normal faults: What are the implications for geometry and production response? Geological Society Special Publications: Industrial Structural Geology: Principles, Techniques and Integration., 421. ISSN: 0305-8719

https://doi.org/10.1144/SP421.12

The missing complexity in seismically imaged normal faults: What are the implications for geometry and production response?

Alan M. Wood [1,2], Douglas A. Paton[1], Richard E.Ll. Collier[1]*
[1]Basin Structure Group, School of Earth and Environment, University of Leeds, Leeds LS2 9JT, United Kingdom
[2] Current address: Shell Global Solutions Netherlands, Rijswijk, Netherlands
**Corresponding author (e-mail: d.a.paton@leeds.ac.uk)*

Abbreviated title: Complexity in seismically imaged faults
Keywords: seismic resolution; normal faults; forward modelling; fluid flow simulation

Abstract

The impact of geometric uncertainty on across-fault flow behaviour at the scale of individual intra-reservoir faults is investigated in this study. A high resolution digital elevation model (DEM) of a faulted outcrop is used to construct an outcrop-scale geocellular grid capturing high-resolution fault geometries (5 m scale). Seismic forward modelling of this grid allows generation of a 3D synthetic seismic cube, which reveals the corresponding seismically resolvable fault geometries (12.5 m scale). Construction of a second geocellular model, based upon the seismically resolvable fault geometries, allows comparison with the original outcrop geometries. Running fluid flow simulations across both models enables us to assess quantitatively the impact of outcrop resolution versus seismic resolution fault geometries upon across-fault flow. The results suggest that seismically resolvable fault geometries significantly underestimate the area of across-fault juxtaposition relative to realistic fault geometries. In turn this leads to overestimates in the sealing ability of faults, and inaccurate calculation of fault plane properties such as transmissibility multipliers (TMs).

Introduction

The use of outcrop analogues for understanding geological uncertainty in hydrocarbon reservoirs has been common practice for many years. With the advent and widespread use of geological modelling software, significant work has been conducted that aims to integrate analogue data within subsurface models (Bryant *et al*. 2000; McCaffrey *et al*. 2005; Paton *et al*. 2007; Jones *et al*. 2009; Pringle *et al.* 2010). Forward modelling the seismic response of geological outcrops can be applied as a tool for understanding the constraints that the finite resolution of seismic data places on our interpretation of subsurface geology. Previously, it has primarily been used for understanding facies architectural geometries (Hodgetts & Howell 2000; Janson *et al*. 2007; Bakke *et al*. 2008; Armitage & Stright 2010; Falivene *et al*. 2010; Tomasso *et al*. 2010) and to enable the integration of geological and reservoir engineering disciplines in characterizing the flow response across specific outcrops (Howell *et al*. 2008; Jackson *et al*. 2009; Rotevatn *et al*. 2009a, b; Rotevatn & Fossen 2011; Adams *et al*. 2011).

The complexity of normal fault geometries is well documented and is attributed to a number of factors including fault growth and linkage resulting in the formation and destruction of relay ramps, complex slip surfaces, fault drag and the role of mechanical stratigraphy; and these can occur at a range of scales (Childs *et al*. 1997, 2009; Willemse 1997; Gupta *et al*. 1998; Gupta & Scholz 2000; McLeod *et al*. 2000; Paton & Underhill 2004; Paton 2006; Ferrill & Morris 2008; Welch *et al*. 2009). Consequently, seismically resolvable across-fault reservoir juxtapositions are likely to differ significantly from those that are present in the subsurface at the reservoir scale. Although these factors are inherent when structural uncertainty is considered (Johansen *et al*. 1994; Townsend *et al*. 1998; Alaei & Petersen 2007), a quantitative comparison of outcrop- and seismically-resolvable fault geometry has so far been lacking, as have the implications of the fault geometry on reservoir simulation.

In this study, for the first time, we consider the discrepancy between seismically resolvable normal faults with outcrop geometry in 3-dimensions using forward seismic modelling techniques (Fig. 1). We then compare the simulated production response across both of the fault geometry resolutions and consider the implications of the reduction in resolution for intra-reservoir scale faults in production settings (Fig. 2).

Methodology

The methodology we employ requires a comparison of the simulated production in a faulted reservoir at outcrop- and seismic-resolutions (Fig. 2). Prior to the simulation we derive the seismic forward model (Fig. 3). We outline both workflows below.

Construction of the geocellular model

Input DEM and its limitations. To characterise fault geometry at a sub-metre reservoir scale a high resolution digital elevation model (DEM) from the Afar Rift system has been used (Fig. 4). The Afar depression in northern Ethiopia began to form at approximately 30 Ma (Barberi & Varet 1977) at the triple junction between the Gulf of Aden, Red Sea and East African Rifts. The depression hosts a range of tectonic regimes including the Dabbahu magmatic segment (Hayward & Ebinger 1996; Rowland *et al*. 2007) where the DEM is located. We choose this area because of the availability of a high resolution data set but also because the topographic surface represents a surface devoid of either significant erosion or deposition, thereby representing accurate hangingwall and footwall cut-offs.

The DEM is derived from an airborne Lidar survey with a spatial resolution of approximately 0.5m, which is at least an order of magnitude greater resolution than high quality reflection seismic data (Hofmann, 2013). This level of resolution reveals outcrop-scale detail, which would be obscured by Fresnel zone effects in seismic data, allowing fault structure and displacement to be accurately captured. Numerous ‘reservoir scale’ fault sets with resolvable displacements of up to 40m are present in the area. The individual segments comprising each fault set are laterally connected via relay zone linkages displaying various stages of evolution and display a range of structures from soft-linked open relays through to fully breached relays with almost continuous displacements. As would be expected, fault architecture complexity is greatest in the vicinity of relay zones where displacement is accommodated across multiple slip surfaces.

We construct the geocellular model at two resolutions (Fig. 2). The first is generated directly from the DEM (the outcrop-resolution model) whereas the second is a seismic forward modelled volume derived from the DEM to replicate a reservoir scenario (the seismic-resolution model). For both resolutions we consider both partially and fully breached relay ramp geometries. We recognise that our models are derived from the extrapolation of a 2D surface and represent a 2.5D rather than a full 3D volume. Although this is a simplification, this leads to our results underestimating the degree of complexity, a point that we discuss subsequently.

Seismic forward modelling. Derivation of the seismic model involves a multi-stage workflow (Fig. 3). The DEM, which has dimensions of approximately 400 x 400 m, is translated to a depth typically analogous to a hydrocarbon reservoir (3500m) and forms the basis of the model (Fig. 3b). The horizontal cell dimensions of 5 m are specified to provide manageable simulation runs although the loss of resolution associated with this grid cell dimension is minimised by careful location of cell nodes using the higher resolution DEM as a guide (Fig. 3c). Vertical grid dimensions are set at 1.5m. For both geometric models we model four stratigraphic scenarios (Fig. 3d):

a) We model two reservoir interval thicknesses of 10m and 30m underlain and overlain by impermeable shales (Figs. 3d(i) and 3d(ii)). These thicknesses represent scenarios where the reservoir is thinner and thicker than the mean cumulative fault throw respectively, and are referred to as high and low thickness to throw ratios (Th:tw).

b) For the two scenarios above we populate the models with two separate sets of petrophysical properties (Porosity, Permeability, VClay), firstly representing a homogenous clean sandstone, and secondly a vertically heterogeneous stratigraphy based on proprietary North Sea well data through a Brent group reservoir (Figs. 3d(iii) and 3d(iv) respectively).

Having established our 4 stratigraphic scenarios for both geometric models we populate the geollecular grids with appropriate petrophysical properties (Table 1). These properties include realistic northern North Sea mineralogical volumetric fractions and factors such as VSand and VShale, as well as pore pressure, which is defined as being approximately 22 MPa above the hydrostatic gradient. Homogenous fluid saturations with no transition zone have been modelled for simplicity.

The populated geocellular grids are exported to seismic forward modelling software (SeisRox, Norsar) where the mineralogical compositions and porosity are used to calculate the solid density assuming a Reuss mixing model (Fig. 3e; Reuss 1929). Gassmann’s theory (Gassmann 1951) is then applied along with the fluid properties (Table 1) and saturation distribution to determine the elastic properties of the model, with reflectivity subsequently calculated using the Zoeppritz equations (Zoeppritz 1919). A 3D seismic survey geometry is defined (Fig. 3f) and a coarser resolution overburden model is constructed to account for wave propagation through the subsurface for a given input wavelet (Fig. 3g). The geological, elastic and reflectivity properties are combined with the background model and survey design, and a simulated pre-stack local imaging (SimPLI™) algorithm (Gjøystdal *et al*. 2007) is applied to generate a synthetic pre-stack depth-migrated 3D seismic cube (Fig. 3g).

Synthetic volume interpretation and modelling. Reflections within the synthetic seismic volumes, which correspond to key horizons, are interpreted in geomodelling software with a range of surface attributes such as coherency, edge detection and dip azimuth applied to aid fault interpretation (Fig. 3h; Townsend *et al*. 1998, Freeman *et al*. 2010). Faults are picked on every trace (approximately 10m spacing) to maximise lateral resolution and to maintain a consistent interpretation methodology. The seismically resolvable fault and horizon geometries are used to construct geocellular grids at the same dimensions and these are populated with the same properties as the detailed grids from which they are derived (Fig. 3i).

Assigning fault rock properties. Within the geocellular models these properties are used to calculate the fault rock properties used during reservoir simulation. It is assumed that fault clay content (as defined by the shale gouge ratio (SGR) algorithm; Yielding *et al*. 1997) is the primary control on fault rock permeability reduction relative to the host stratigraphy; other mechanisms such as clay smearing and cataclasis are not considered. Low-, mid- and high-seal case fault transmissibility multipliers (Knai & Knipe 1998; Manzocchi *et al*. 1999) are calculated by employing three separate clay contents to permeability transforms based on those of Manzocchi *et al*. (1999), Jolley *et al*. (2007) and Sperrevik *et al*. (2002) respectively. These represent high-, mid-, and low-fault rock permeability respectively. Fault threshold pressures of 5.9 bar have been assigned based on mean SGR values for the suite of models, and the relationship defined by Bretan *et al*. (2003). To avoid introducing complicating variables this value has been kept constant for all faults across all models.

Flow simulations

Following generation of both outcrop-resolution and seismic-resolution grids, the effect of the discrepancies between the two geometries upon across-fault flow can be quantified using flow simulations (Fig. 2). Simulation is performed using the Eclipse^{TM} black oil simulator (Schlumberger), with a 12 year waterflood development strategy consisting of a single injection well in the hangingwall and a single production well in the footwall. Maximum production rates have been set as 50 sm^3/day for oil and 250 sm^3/day for produced water (i.e. an 83% water cut), with injection rates set to match oil production rates (Table 1). These rates are broadly consistent with both the production data from the proprietary dataset used to populate the stratigraphy, and similar simulation-based studies (Rotevatn *et al*. 2009a, b; Rotevatn & Fossen 2011). To minimise compositional effects the bottom-hole pressure has been set to prevent the bubble point pressure from being reached during pressure depletion of the reservoir. Aquifer support consists of a Carter-Tracy aquifer (Batycky *et al*. 2007) with drive from the down-dip hangingwall, as would be expected for a tilted fault block trap geometry.

Results

In total, 8 different geocellular models are generated: 2 x resolution (outcrop resolution versus seismic resolution); 2 x geometry (partially breached versus fully breached); 2 x reservoir thickness (high and low Th:tw); and 2 x reservoir heterogeneity (homogenous versus heterogeneous). For each of these models 3 different TM scenarios (high, mid and low case) are simulated. Although we do not show all of the models here, we summarize the main differences in geometry and production results amongst them.

Fault geometry

The simplest comparison is the geometric difference for a partially breached relay ramp between the outcrop-resolution and the seismic-resolution case (Fig. 5). Not surprisingly, the fault geometries in the former are significantly more complex than the latter. Faults in the seismic-resolution model generally consist of a single fault plane, which accommodates all of the fault displacement with sub-seismic faulting being imaged as hangingwall deformation and folding, as is the case in the example presented.

This complex fault architecture, which is below seismic resolution, reveals that displacement is distributed across multiple slip surfaces, with this partitioning and complexity, including fault lenses and faulted relay zones, being a direct result of fault growth processes (Childs *et al*. 2009). These are also likely to be poorly imaged due to diffraction effects (Townsend *et al*. 1998).

A representative selection of the other scenarios, including a breached relay ramp and variations in throw:thickness ratio are shown in Figure 6. Although the difference between the outcrop- and seismic-resolution models is most pronounced for the partially breached relay ramp (Fig. 5 and Fig. 6a), it is important to note that it is not just the geometry that plays a role in the final model, but also the stratigraphy. As an example, in the partially breached geometry at seismic-resolution the presence of a thinner reservoir interval (Fig. 6a) provides sufficient amplitude impedance that a significant amount of the smaller scale faulting is imaged around the relay ramp. In contrast, for the thicker reservoir interval (Fig. 6b) although the input geometry is the same the thicker interval results in a less defined impedance contrast, which reduces the detail in the imaging of the fault zone.

For the breached relay ramp example the differences are less pronounced (Figs. 6c and 6d). In all scenarios the fault is relatively consistently defined and the main difference is the degree to which local fault plane asperities and hangingwall/footwall deformation are defined.

Effective juxtaposition

Although qualitative comparisons are insightful (e.g. Figs. 5 and 6), we can also quantify the differences between our scenarios. The effective juxtaposition area is defined as the area of across-fault self-juxtaposition of the reservoir interval that provides a direct or indirect flow pathway between the hangingwall and footwall. For both partially breached and fully breached geometries (Figs. 6 and 7) the effective juxtaposition area is significantly lower for the seismic-resolution fault geometries than the outcrop-resolution, reflecting the limited resolution of the seismic data.

In order to quantify the influence of geometry and throw versus reservoir interval thickness we calculate the absolute effective areas for outcrop-resolution and seismic-resolution models (Fig. 7; fault dimensions in both scenarios have been equalized to allow for comparisons). Juxtaposition area across parts of faults contained entirely within either the main footwall or hangingwall blocks (e.g. fault tips and splays) do not contribute although these minor faults may still effect the overall sweep pattern of the reservoir.

The magnitude of this effect is significantly greater where the vertical thickness of the reservoir interval is less than the mean cumulative fault throw (low Th:tw). As a consequence, low Th:tw configurations are often modelled with the reservoir interval being completely offset, hence resulting in apparently widespread juxtaposition sealing. In contrast the architectural complexity of high-resolution fault geometries, as defined by our outcrop examples, leads to maintenance of across-fault juxtaposition, even for low Th:tw situations (Fig. 6).

The difference in juxtaposition area is amplified where there is a low Th:tw, since a lower throw is required to completely offset the reservoir and result in a juxtaposition seal. The absolute values of effective juxtaposition area are higher for the partially breached geometries than the fully breached geometries. Again, this is a result of fault growth processes with profile readjustment of the hard-linked faults leading to increased throw across the relay and hence lower juxtaposition areas being maintained. In addition, as throw localizes onto the through-going structure small-scale faults and splays are abandoned in the footwall or hangingwall and hence do not contribute to the effective juxtaposition area.

Simulation models

We now consider how the observed variation in effective juxtaposition in the multiple scenarios influences simulated production rates and fluid saturations.

Production rates. The effects on simulated production of the disparities in juxtaposition area can be significant, with final cumulative produced volumes varying by over a factor of 4 (Fig. 7). The production curves also illustrate the differences between outcrop and seismically resolvable geometries for high and low Th:tw ratios and low-, mid- and high-case fault rock permeability.

Where a high Th:tw is modelled the effective juxtaposition areas are of the same order of magnitude for both outcrop (Fig. 7a) and seismically-resolvable (Fig. 7b) geometries, leading to virtually no difference in the simulated production results regardless of the different fault TMs. In contrast, where a low Th:tw is modelled, the effective juxtaposition area is over an order of magnitude lower for the seismically-resolvable geometry (Fig. 7d) than for the outcrop-derived geometry (Fig. 7c), leading to significant variations in the simulation results.

The architectural complexity of the outcrop-resolution geometries leads to in excess of an order of magnitude greater effective juxtaposition area than the seismically resolvable geometries, and hence to multiple potential flow pathways being preserved. Although the different TMs do lead to variations in the onset of production decline, over the course of the simulations the cumulative produced volumes are similar. This differs from the seismically resolvable geometries, where production rates and cumulative volumes vary significantly over the course of the simulations.

The high-case fault TMs (low permeability) lead to restricted across-fault flow and hence low production rates compared to the mid- and low-case TMs.

Fluid saturations. The impact of varying the juxtaposition area and the fault TMs is also manifested by the fluid saturation distribution (Fig. 8). For the outcrop-derived geometries there is increased focussing of flow up the relay zone with decreasing fault rock permeability (high-case TMs), since the relay zone offers the path of least resistance. This is true for both high and low Th:tw, although more apparent for low Th:tw. Despite this, for the outcrop-derived geometries the saturation distributions are broadly consistent irrespective of the fault TMs used (Fig. 8). Conversely the saturations for the geometries resolvable in the seismic data vary vastly at any one simulation timestep, depending on the different fault geometries (and hence juxtaposition area) and the different fault TMs. Where a high Th:tw is modelled, varying the fault TMs has very little impact, whereas a low Th:tw leads to significant variation in the simulated fluid distribution. In this situation the high- and mid-case TMs reduce across-fault flow and hence impede the replacement of oil with water in the hangingwall. The low-case TMs, however, have little impact on flow retardation, with production simulation results being very similar to the outcrop-derived geometry.

Influence of varying net:gross

The initial models employed a stratigraphy where the reservoir interval had a constant net to gross ratio of 1 (Fig. 3). Vertical connectivity was not as restricted as would be the case for an interbedded sequence of permeable and impermeable layers (e.g. Fig. 3d). In such vertically stratified sequences faults can significantly enhance vertical permeability by juxtaposing otherwise separate layers (Manzocchi *et al*. 2010). To test the impact of fault geometric uncertainty in these situations, a series of models for both outcrop- and seismic-resolution geometries have been constructed with the net:gross ratio ranging between 0.14 and 0.46 (Fig. 9 shows representative outcrop-resolution models). The effective juxtaposition area increases with net:gross, although it remains consistently higher for the outcrop-resolution geometry (Figs. 9a and 9c).

Intuitively it would be expected that the mean SGR values on these juxtaposition windows would decrease with increasing net:gross since overall there is less shale within the sequence, however this is not the case. Instead a more complex, less predictable pattern of mean SGR values emerges, especially for the outcrop-derived geometry. At the lowest values of net:gross the majority of juxtaposition windows occur where the throw is less than the thickness of the individual layers, for example towards fault tips (Fig. 9b). A minimal volume of shale has therefore passed the fault and hence low SGR values result. In contrast, where moderate net:gross ratios have been modelled (Fig. 9c), a greater area of juxtaposition occurs, however a larger proportion of shale has passed these windows and results in a higher SGR value.

The role of fault TMs and fault geometry on production is also considered (Fig. 10). Where low-case (high permeability) fault TMs are specified (Fig. 10a) the disparity in juxtaposition area between the two geometries has less impact on the simulated production, since the low-case fault TMs do not excessively restrict across-fault flow. Therefore, for any given net:gross ratio the difference between the outcrop-resolution and seismic-resolution geometries is less than for the cases with lower permeability fault rocks (Fig. 10c).
In contrast, where high-case TMs are employed (Fig. 10c) the cumulative production volume is consistently lower for the seismically resolvable geometry than for the outcrop-derived geometry, irrespective of the net:gross of the stratigraphy. This indicates that the low permeability of the fault rocks, combined with the lower juxtaposition areas of the seismically resolvable geometry, is severely restricting across-fault flow. This emphasizes that the predicted impact of faults upon fluid flow within reservoirs based upon their seismically resolvable geometries may vary significantly compared to their impact when realistic geometries (and hence juxtaposition areas) are accounted for.

Vertical permeability

Although a number of our models utilize a well-derived, vertically layered permeability distribution, within each individual layer the permeability values are isotropic. It is common however for vertical to horizontal permeability ratios (Kv:Kh) to be significantly lower than 1, due to compaction and preferential alignment of grains during burial. This leads to the impediment of layer-perpendicular fluid flow which restricts hydraulic connectivity of vertically separated layers. Previous work (Manzocchi *et al*. 2010) has shown the importance of fault structure in enhancing vertical connectivity in low Kv:Kh sequences. The relative impact of varying the Kv:Kh on the simulated production response of outcrop and seismically resolvable fault geometries has been assessed by running simulations across 6 orders of magnitude of Kv:Kh (Manzocchi *et al*. 2010) (Fig. 11). Mid-case fault TMs have been assigned for all scenarios. For both geometries a lower Kv:Kh results in a lower cumulative production volume, with the absolute produced volumes being lower for the seismically resolvable geometry compared to the outcrop-derived geometry. The results for the seismically resolvable geometry also display significantly more variation than those of the outcrop-derived geometry. As already seen, outcrop fault geometries are significantly more complex than those resolved within seismic data. This complexity enhances vertical connectivity by allowing across-fault juxtaposition of otherwise vertically separated areas, and hence leads to less disparity between high and low ratio Kv:Kh stratigraphies. As a result the limited across-fault juxtaposition area of the seismically resolvable geometries restricts the vertical connectivity and leads to greater variability between the different Kv:Kh ratio stratigraphies. This suggests that determining the correct Kv:Kh may be less important than simulations based upon seismically resolvable fault geometries would imply.

Implications

Faults are almost universally represented within geocellular models, and by extension, fluid flow simulators as simple, single slip surfaces. The reason for this is both an issue of data resolution and of the limitations in incorporating faults within geocellular grids. However, fault growth processes necessitate that fault architecture is significantly more complex than the geometries resolvable in, and modelled from, seismic data. As a result, fault and simulation models that are constructed based upon seismically resolvable fault geometries are unlikely to behave in the same way with regards to across-fault fluid flow as would the complex fault geometries present in the subsurface.

A number of different approaches may aid and improve the accuracy of simulations where faults are present. A variety of techniques exist for predicting fault architecture based upon the burial history and geomechanical properties of the stratigraphy, however these are generally restricted to two dimensions (e.g. Welch *et al*. 2012). Difficulties arise in incorporating this complexity into large reservoir models, where horizontal grid-cell dimensions may typically be on the order of 200m. Locally refining the grid to a level of detail which allows the complexity to be captured often leads to prohibitively long simulation run times (Manzocchi *et al*. 2008).

Incorporating the vertical heterogeneity in fault structure is even less straightforward given the way geocellular grids are constructed in the majority of reservoir modelling software packages. Indeed, as outlined previously, our models correspond to a high resolution 2.5D model rather than a full 3D volume. Were it possible to capture and subsequently model the full 3D geometry of faults it is likely that the additional heterogeneity encountered would lead to even greater levels of across-fault juxtaposition than our 2.5D approximations.

An alternative approach to including fault geometries and properties deterministically is to incorporate complexity via a conditioned semi-stochastic or probabilistic methodology (Odling *et al*. 2005; Rivenæs *et al*. 2005; Childs *et al*. 2007; Manzocchi *et al*. 2008; Yielding 2012). Although this approach has a number of potential pitfalls, especially where a laterally heterogeneous stratigraphy is present, it may provide more accurate predictive simulations of fluid flow. Perhaps the simplest approach to account for geometric complexity is to stochastically include sub-seismic relay zones (Manzocchi *et al*. 2008) which provide across-fault flow pathways.

Our results have indicated that across-fault juxtaposition area is likely to be severely underestimated when based on seismically resolvable fault geometries, potentially leading to faults being modelled as overly retardant to flow. Nevertheless certain scenarios, such as shale-rich, low net:gross reservoirs, may indeed experience juxtaposition-restricted across-fault flow. Under these conditions the relative importance of the fault rock properties on influencing across-fault transmissibility increases, with significant variability observed where different clay content to permeability transforms are applied. These permeability transforms are dependent on a number of variables including the specific burial history, hence applying a locally calibrated clay content to permeability transform is critical where limited across-fault juxtaposition area exists.

Relative importance of fault zone structure versus fault rock properties

Our simulation results suggest that it is the juxtaposition area that is the most critical factor in controlling across-fault fluid flow, with fault rock properties being of subordinate importance. For high-resolution fault geometries, with large juxtaposition areas, there is minimal difference in simulated results irrespective of the fault TMs which are applied. Conversely the seismically resolvable geometries, with low juxtaposition areas, display significant variation between different fault TM scenarios. This leads to the most important implication, that seismically resolvable fault geometries are often modelled as being too sealing, since they underestimate the juxtaposition area available to accommodate across-fault flow. This also leads to erroneous emphasis being placed on the influence of fault rock properties on fluid flow. Indeed, since the calculation of SGR-based fault TMs is dependent on fault throw, it is likely that the fault TMs applied to seismically resolvable fault geometries may be inappropriate.

Conclusions

For the first time we use a high resolution DEM to generate a 3D synthetic seismic cube in order to compare geometry, petrophysical properties and flow simulation on normal faults at high resolution and at seismic resolution. Our findings show:

- Fault geometries identifiable in seismic data are significantly simplified relative to those observed at outcrop and this reduction is most noticeable in partially breached relay ramps.
- The simplified geometry leads to a severe underestimate in the area of across-fault self-juxtaposition of reservoir intervals for seismically resolvable faults, with the magnitude of this disparity being amplified where the reservoir thickness is less than the mean fault throw.
- Large juxtaposition areas, regardless of whether they are within the outcrop or seismic model, lead to limited differences in the across-fault flux of hydrocarbon irrespective of the fault transmissibility multipliers which are applied.
- With a relatively permeable fault rock only a small juxtaposition ‘window’ is required to dominate across-fault fluid flow. This leads to a similar production response to situations with significantly larger juxtaposition areas. Identifying potential ‘windows’ is therefore critical when attempting to predict across-fault flow behaviour.

We conclude that across-fault fluid flow is, therefore, in part controlled by a combination of both juxtaposition area and fault permeability. Fault geometries modelled from seismic data will underestimate the juxtaposition area available for across-fault flow, often leading to faults being modelled as overly sealing even when appropriate fault permeabilities are included. This emphasizes the importance of careful mapping of faults geometries when assessing reservoir performance. Ideally multiple realizations, rather than a single realization, of fault geometry would be included in reservoir uncertainty analysis.

Acknowledgements

This work has been made possible thanks to NERC PhD studentship funding for A. Wood, as well as an additional CASE monetary contribution and support from Shell. We are very grateful to Woody Wilson and Clare Bond for very helpful reviews and Nick Richardson for editorial advice. We would like to thank Schlumberger for providing academic licences for Petrel and Norsar for SeiSrox.

References

ADAMS, E. W., GRÉLAUD, C., PAL, M., CSOMA, A. É., AL JA'AIDI, O. S. & HINAI, R. A. 2011. Improving reservoir models of Cretaceous carbonates with digital outcrop modelling (Jabal Madmar, Oman): static modelling and simulating clinoforms. *Petroleum Geoscience,* 17, 309-332.

ALAEI, B. & PETERSEN, S. A. 2007. Geological modelling and finite difference forward realization of a regional section from the Zagros fold-and-thrust belt. *Petroleum Geoscience,* 13, 241-251.

ARMITAGE, D. A. & STRIGHT, L. 2010. Modeling and interpreting the seismic-reflection expression of sandstone in an ancient mass-transport deposit dominated deep-water slope environment. *Marine and Petroleum Geology,* 27, 1-12.

BAKKE, K., GJELBERG, J. & AGERLIN PETERSEN, S. 2008. Compound seismic modelling of the Ainsa II turbidite system, Spain: Application to deep-water channel systems offshore Angola. *Marine and Petroleum Geology,* 25, 1058-1073.

BARBERI, F. & VARET, J. 1977. Volcanism of Afar: Small-scale plate tectonics implications. *Geological Society of America Bulletin,* 88, 1251-1266.

BATYCKY, R.P., THIELE, M.R., COATS, K.H., GRINDHEIM, A., PONTING, D., KILLOUGH, J.E., SETTARI, T., THOMAS, K.L., WALLIS, J., WATTS, J.W. & WHITSON C.H. 2007. Reservoir Engineering and Petrophysics. 17 Reservoir Simulation. V-1399. In: Petroleum Engineering Handbook, Volume V, Holstein, E.D. (ed). 2007. Society of Petroleum Engineers.

BRETAN, P., YIELDING, G. & JONES, H. 2003. Using calibrated shale gouge ratio to estimate hydrocarbon column heights. *AAPG Bulletin,* 87, 397-413.

BRYANT, I., CARR, D., CIRILLI, P., DRINKWATER, N., MCCORMICK, D., TILKE, P. & THURMOND, J. 2000. Use of 3D digital analogues as templates in reservoir modelling. *Petroleum Geoscience,* 6, 195-201.

CHILDS, C., MANZOCCHI, T., WALSH, J. J., BONSON, C. G., NICOL, A. & SCHÖPFER, M. P. J. 2009. A geometric model of fault zone and fault rock thickness variations. *Journal of Structural Geology,* 31, 117-127.

CHILDS, C., WALSH, J. J., MANZOCCHI, T., STRAND, J., NICOL, A., TOMASSO, M., SCHOPFER, M. P. J. & APLIN, A. C. 2007. Definition of a fault permeability predictor from outcrop studies of a faulted turbidite sequence, Taranaki, New Zealand. *Geological Society, London, Special Publications,* 292, 235-258.

CHILDS, C., WALSH, J. J. & WATTERSON, J. 1997. Complexity in fault zone structure and implications for seal prediction. *In:* MØLLER-PEDERSEN, P. & KOESTLER, A. G. (eds.) *Hydrocarbon Seals: Importance for Exploration and Production.Norwegian Petroleum Society Special,* 7, 61-72.

FALIVENE, O., ARBUÉS, P., LEDO, J., BENJUMEA, B., MUÑOZ, J. A., FERNÁNDEZ, O. & MARTÍNEZ, S. 2010. Synthetic seismic models from outcrop-derived reservoir-scale three-dimensional facies models: The Eocene Ainsa turbidite system (southern Pyrenees). *AAPG Bulletin,* 94, 317-343.

FERRILL, D. A. & MORRIS, A. P. 2008. Fault zone deformation controlled by carbonate mechanical stratigraphy, Balcones fault system, Texas. *AAPG Bulletin,* 92, 359-380.

FREEMAN, S. R., HARRIS, S. D. & KNIPE, R. J. 2010. Cross-fault sealing, baffling and fluid flow in 3D geological models: tools for analysis, visualization and interpretation. *Geological Society, London, Special Publications,* 347, 257-282.

GASSMANN, F. 1951. On the Elasticity of Porous Media. *Vierteljahrsschrift der Naturforschenden Gesellschaft in Zurich,* 96, 1-23.

GJØYSTDAL, H., DROTTNING, Å., LECOMTE, I. & BRANSTON, M. 2007. Advances in quantitative model-assisted seismic interpretation. *First Break,* 25, 95-102.

GUPTA, A. & SCHOLZ, C. H. 2000. A model of normal fault interaction based on observations and theory. *Journal of Structural Geology,* 22, 865-879.

GUPTA, S., COWIE, P. A., DAWERS, N. H. & UNDERHILL, J. R. 1998. A mechanism to explain rift basin subsidence and stratigraphic patterns through fault-array evolution. *Geology,* 26, 595-598.

HAYWARD, N. J. & EBINGER, C. J. 1996. Variations in the along-axis segmentation of the Afar Rift system. *Tectonics,* 15, 244-257.

HODGETTS, D. & HOWELL, J. A. 2000. Synthetic seismic modelling of a large-scale geological cross-section from the Book Cliffs, Utah, USA. *Petroleum Geoscience,* 6, 221-229.

HOFMANN, B., 2013. How do faults grow in magmatic rifts? LiDAR and InSAR observations of the Dabbahu rift segment, Afar, Ethiopa. University of Leeds PhD Thesis. 169 pp.

HOWELL, J. A., SKORSTAD, A., MACDONALD, A., FORDHAM, A., FLINT, S., FJELLVOLL, B. & MANZOCCHI, T. 2008. Sedimentological parameterization of shallow-marine reservoirs. *Petroleum Geoscience,* 14, 17-34.

JACKSON, M. D., HAMPSON, G. J. & SECH, R. P. 2009. Three-dimensional modeling of a shoreface-shelf parasequence reservoir analog: Part 2. Geologic controls on fluid flow and hydrocarbon recovery. *AAPG Bulletin,* 93, 1183-1208.

JANSON, X., KERANS, C., BELLIAN, J. A. & FITCHEN, W. 2007. Three-dimensional geological and synthetic seismic model of Early Permian redeposited basinal carbonate deposits, Victorio Canyon, west Texas. *AAPG Bulletin,* 91, 1405-1436.

JOHANSEN, S. E., KIBSGAARD, S., ANDRESEN, A., HENNINGSEN, T. & GRANLI, J. R. 1994. Seismic modeling of a strongly emergent thrust front, West Spitsbergen fold belt, Svalbard. *AAPG Bulletin,* 78, 1018-1027

JOLLEY, S. J., DIJK, H., LAMENS, J. H., FISHER, Q. J., MANZOCCHI, T., EIKMANS, H. & HUANG, Y. 2007. Faulting and fault sealing in production simulation models: Brent Province, northern North Sea. *Petroleum Geoscience,* 13, 321-340.

JONES, R. R., MCCAFFREY, K. J. W., CLEGG, P., WILSON, R. W., HOLLIMAN, N. S., HOLDSWORTH, R. E., IMBER, J. & WAGGOTT, S. 2009. Integration of regional to outcrop digital data: 3D visualisation of multi-scale geological models. *Computers & Geosciences,* 35, 4-18.

KNAI TA; KNIPE RJ (1998) The impact of faults on fluid flow in the Heidrun Field, In: Jones G; Fisher QJ; Knipe RJ (Ed) *Faulting and fault sealing and fluid flow in hydrocarbon reservoirs*, Geological Society Special Publication, 147, Geological Society of London, pp.269-282.

MANZOCCHI, T., CHILDS, C. & WALSH, J. J. 2010. Faults and fault properties in hydrocarbon flow models. *Geofluids*, 10, 94-113.

MANZOCCHI, T., HEATH, A. E., PALANANTHAKUMAR, B., CHILDS, C. & WALSH, J. J. 2008. Faults in conventional flow simulation models: a consideration of representational assumptions and geological uncertainties. *Petroleum Geoscience,* 14, 91-110.

MANZOCCHI, T., WALSH, J. J., NELL, P. & YIELDING, G. 1999. Fault transmissibility multipliers for flow simulation models. *Petroleum Geoscience,* 5, 53-63.

MCCAFFREY, K. J. W., JONES, R. R., HOLDSWORTH, R. E., WILSON, R. W., CLEGG, P., IMBER, J., HOLLIMAN, N. & TRINKS, I. 2005. Unlocking the spatial dimension: digital technologies and the future of geoscience fieldwork. *Journal of the Geological Society,* 162, 927- 938.

MCLEOD, A. E., DAWERS, N. H. & UNDERHILL, J. R. 2000. The propagation and linkage of normal faults: insights from the Strathspey Brent& Statfjord fault array, northern North Sea. *Basin Research,* 12, 263-284.

ODLING, N. E., HARRIS, S. D., VASZI, A. Z. & KNIPE, R. J. 2005. Properties of fault damage zones in siliciclastic rocks: a modelling approach. *Geological Society, London, Special Publications,* 249, 43-59.

PATON, D.A. 2006. Influence of crustal heterogeneity on normal fault dimensions and evolution: southern South Africa extensional system, *Journal of Structural Geology,* 28, 868-886.

PATON, D.A., Carr, M., Trudgill, B., Ortner, H. & Medwedeff, D.A. 2007. Alpine-scale 3D geospatial modelling: Applying new techniques to old problems, *Geosphere*, December 2007, vol.3, p 527-549.

PATON, D.A. & UNDERHILL, J. 2004. Role of crustal anisotropy in modifying the structural and sedimentological evolution of extensional basins: the Gamtoos Basin, South Africa, *Basin Research,* 16, 339-359.

PEACOCK, D. C. P. & SANDERSON, D. J. 1991. Displacements, segment linkage and relay ramps in normal fault zones. *Journal of Structural Geology,* 13, 721-733.

PRINGLE, J. K. B., R. L. HODGSON, D. M. FLINT, S. S. 2010. Capturing stratigraphic and sedimentological complexity from submarine channel complex outcrops to digital 3D models, Karoo Basin, South Africa. *Petroleum Geoscience,* 16, 307-330.

REUSS, A. 1929. Berechnung der Fließgrenze von Mischkristallen auf Grund der Plastizitätsbedingung für Einkristalle. *ZAMM - Journal of Applied Mathematics and Mechanics / Zeitschrift für Angewandte Mathematik und Mechanik,* 9, 49-58.

RIVENÆS, J. C., OTTERLEI, C., ZACHARIASSEN, E., DART, C. & SJØHOLM, J. 2005. A 3D stochastic model integrating depth, fault and property uncertainty for planning robust wells, Njord Field, offshore Norway. *Petroleum Geoscience,* 11, 57-65.

ROTEVATN, A., BUCKLEY, S. J., HOWELL, J. A. & FOSSEN, H. 2009a. Overlapping faults and their effect on fluid flow in different reservoir types: A LIDAR-based outcrop modelling and flow simulation study. *AAPG Bulletin,* 93, 407-427.

ROTEVATN, A. & FOSSEN, H. 2011. Simulating the effect of subseismic fault tails and process zones in a siliciclastic reservoir analogue: Implications for aquifer support and trap definition. *Marine and Petroleum Geology,* 28, 1648-1662

ROTEVATN, A., TVERANGER, J., HOWELL, J. A. & FOSSEN, H. 2009b. Dynamic investigation of the effect of a relay ramp on simulated fluid flow: geocellular modelling of the Delicate Arch Ramp, Utah. *Petroleum Geoscience,* 15, 45-58.

ROWLAND, J. V., BAKER, E., EBINGER, C. J., KEIR, D., KIDANE, T., BIGGS, J., HAYWARD, N. & WRIGHT, T. J. 2007. Fault growth at a nascent slow-spreading ridge: 2005 Dabbahu rifting episode, Afar. *Geophysical Journal International,* 171, 1226-1246.

SPERREVIK, S., GILLESPIE, P. A., FISHER, Q. J., HALVORSEN, T. & KNIPE, R. J. 2002. Empirical estimation of fault rock properties. *In:* KOESTLER, A. G. & HUNSDALE, R. (eds.) *Hydrocarbon Seal Quantification. Norwegian Petroleum Society Special Publication*, 11, 109-125.

TOMASSO, M., BOUROULLEC, R. & PYLES, D. R. 2010. The use of spectral recomposition in tailored forward seismic modeling of outcrop analogs. *AAPG Bulletin,* 94, 457-474.

TOWNSEND, C., FIRTH, I. R., WESTERMAN, R., KIRKEVOLLEN, L., HARDE, M. & ANDERSEN, T. 1998. Small seismic-scale fault identification and mapping. *Geological Society, London, Special Publications,* 147, 1-25.

WELCH, M. J., DAVIES, R. K., KNIPE, R. J. & TUECKMANTEL, C. 2009. A dynamic model for fault nucleation and propagation in a mechanically layered section. *Tectonophysics,* 474, 473-492.

WELCH, M., FRISCHBUTTER, A., & . KNIPE, R.J. 2012. The Value of Geomechanical Modelling of Fault Properties for Trap Analysis. Fault and Top Seals Conference, 2012, Montpellier.

WILLEMSE, E. J. M. 1997. Segmented normal faults: Correspondence between threedimensional mechanical models and field data. *J. Geophys. Res.,* 102, 675-692.

YIELDING, G., FREEMAN, B. & NEEDHAM, D. T. 1997. Quantitative fault seal prediction. *AAPG Bulletin,* 81, 897-917.

YIELDING, G. 2012. Using probabilistic shale smear modelling to relate SGR predictions of column height to fault-zone heterogeneity. *Petroleum Geoscience,* 18, 33-42.

ZOEPPRITZ, K. 1919. Erdbebenwellen VII. VIIb. Über Reflexion und Durchgang seismischer Wellen durch Unstetigkeitsflächen. *Nachrichten von der Königlichen Gesellschaft der Wissenschaften zu Göttingen, Mathematisch-physikalische Klasse*, 66-84.

List of tables

Table 1 Physical properties used for generation of elastic and reflectivity cubes during the seismic forward modelling process.

List of figures

Fig. 1. (a) Reservoir scale faults from Utah, USA. The complex fault geometry results in partitioning of displacement across multiple fault planes, leading to the individual units being self-juxtaposed. (b) Typical sub-surface seismic response of the fault structure shown in (a).

The image shown in (a) is superimposed for reference. Note the lack of resolvable detail. The preclusion of detailed imaging of fault structure generally leads to faults being modelled as simple two-dimensional planes. Uncertainty in the position of horizon-fault intersections caused by amplitude deterioration adjacent to faults is tackled by projecting reflectors towards the faults from a set distance.

Fig. 2. Generalized workflow used for comparing simulation results for outcrop-resolution and seismically forward resolution fault geometries. (a) High resolution LIDAR DEM is used to construct a detailed fault model and geocellular grid at a depth of 3500m. This grid is subsequently populated with appropriate petrophysical properties. (b) The populated geocellular grid is exported to forward modelling software where the elastic and reflectivity properties are calculated. These properties are used in conjunction with a background model and seismic survey design to generate a 3D synthetic pre-stack depth-migrated seismic cube. (c) The forward modelled seismic cube is interpreted and the seismically resolvable fault geometries used to construct a second geocellular grid. This grid is populated with the same petrophysical properties as the original, outcrop-derived models. (d) Fluid flow simulation results for both the outcrop-derived and the seismically resolvable geometries allow the differences in across-fault flow which are due to the discrepancies in fault architecture to be identified.

Fig. 3. Specific workflow for generating the seismic forward model from the geological model. a) Input surface from the DEM. b) Geocelullar grid generated from the DEM. c) The geocellular grid is re-sampled into a regular grid with uniform cell dimensions prior to export to forward modelling software. d) Varying petrophysical properties are used to populate the geometries in (c). The reservoir interval is either thicker (i, iii) or thinner (ii, iv) than the mean fault throws. The stratigraphies are either homogeneous (i, ii) or derived from North Sea well data (iii, iv). e) Geocellular grid is imported into forward modelling software and populated with appropriate petrophsyical properties. f) A 3D survey is designed and the dip and azimuth of potentially illuminated reflections calculated. This is combined with an input wavelet and the elastic and reflectivity properties of the target area and of the background model to generate the synthetic seismic cube. g) The synthetic pre-stack depth-migrated (PSDM) seismic cube. h) A standard seismic interpretation workflow is used to generate seismic horizons and fault interpretations. i) A geocellular model is constructed from the seismic interpretation with the same dimensions as the original, detailed model. It is populated with identical petrophysical properties.

Fig. 4. Location map for the digital elevation data used to generate high-resolution fault architectures. The data are located within the Afar rift system, Ethiopia. A number of the rift elements are shown for reference (Rowland *et al*. 2007; Barberi & Varet 1977).

Fig. 5. Example of a) outcrop-resolution and b) seismic-resolution models generated for a partially breached relay zone.

Fig. 6. Oblique view of a selection of the input (outcrop-resolution), synthetic, and output (seismic-resolution) models for 'Top Reservoir' horizon. (a) Thickness < Throw, homogeneous stratigraphy, partially breached relay. (b) Thickness > Throw, heterogeneous stratigraphy, partially breached relay. (c) Thickness < Throw, homogeneous stratigraphy, fully breached relay. (d) Thickness > Throw, heterogeneous stratigraphy, fully breached relay.

Fig. 7. Four different scenarios from Figure 6 to show the influence of resolution and stratigraphy on both effective juxtaposition and production for a partially breached relay ramp. (a) High Th:tw, outcrop fault geometry. (b) High Th:tw, seismically resolvable geometry. (c) Low Th:tw, outcrop fault geometry. (d) Low Th:tw, seismically resolvable geometry. The simulation results highlight the importance of the ratio of stratigraphic thickness to fault throw (Th:tw) in terms of the effective juxtaposition area (shown) for a partially breached relay zone geometry. OPC = Oil Production Cumulative, OPR = Oil Production Rate, Red = High seal TM, Yellow = Mid Seal TM and Green = Low Seal TM.

Fig. 8. Images of fluid saturation part way through the simulation runs for nine different scenarios. Red is low saturation and blue is high saturation. There are limited differences in fluid distribution between the outcrop and seismically resolvable fault geometries and the different fault TMs where there is a high Th:tw, and hence a large juxtaposition area. In contrast the low Th:tw cases show significant differences in fluid saturation distribution for the different fault geometries and different fault TMs.

Fig. 9. Oblique view of partially breached outcrop geometry showing the resulting models populated with (a and b) N:G = 0.14 and (c and d) N:G = 0.46. (b) and (d) show corresponding SGR values with faults shown as a transparency with SGR values superimposed where the reservoir interval is self-juxtaposed. The base reservoir horizon is also shown. In (b) Low N:G (0.14) results in the reservoir only being self-juxtaposed in areas of very low displacement, i.e. at the fault tips. Since these areas have passed little shale during deformation, their corresponding SGR values are low. In contrast, in (d) a higher N:G

(0.46) leads to multiple sections of the reservoir interval being self-juxtaposed. Many of these intervals have passed shale during deformation and hence have higher SGR values.

Fig. 10. Cumulative produced volume from seismically resolvable geometries as a percentage of that of the outcrop geometry for varied N:G ratios. (a) low case TMs, (b) mid case, (c) high case. Higher fault rock permeability (a) leads to less disparity between seismically resolvable and outcrop-derived fault geometries than less permeable fault rocks (c).

Fig. 11. Plots illustrating the impact of vertical to horizontal permeability ratio (Kv:Kh) on cumulative hydrocarbon production for (a) outcrop-derived fault geometry and (b) forward modelled, seismically resolvable fault geometry. The percentage difference between the highest and lowest Kv:Kh ratios is shown by the solid black lines. In both cases lower Kv:Kh results in lower cumulative hydrocarbon production over the course of the simulation runs. The difference between the highest and lowest produced volumes however is significantly greater for the seismically resolvable fault geometries (b, ca. 40%) than the outcrop-derived fault geometries (a, ca. 20%). Note that the absolute produced volumes are also significantly lower for the seismically resolvable geometry (b).

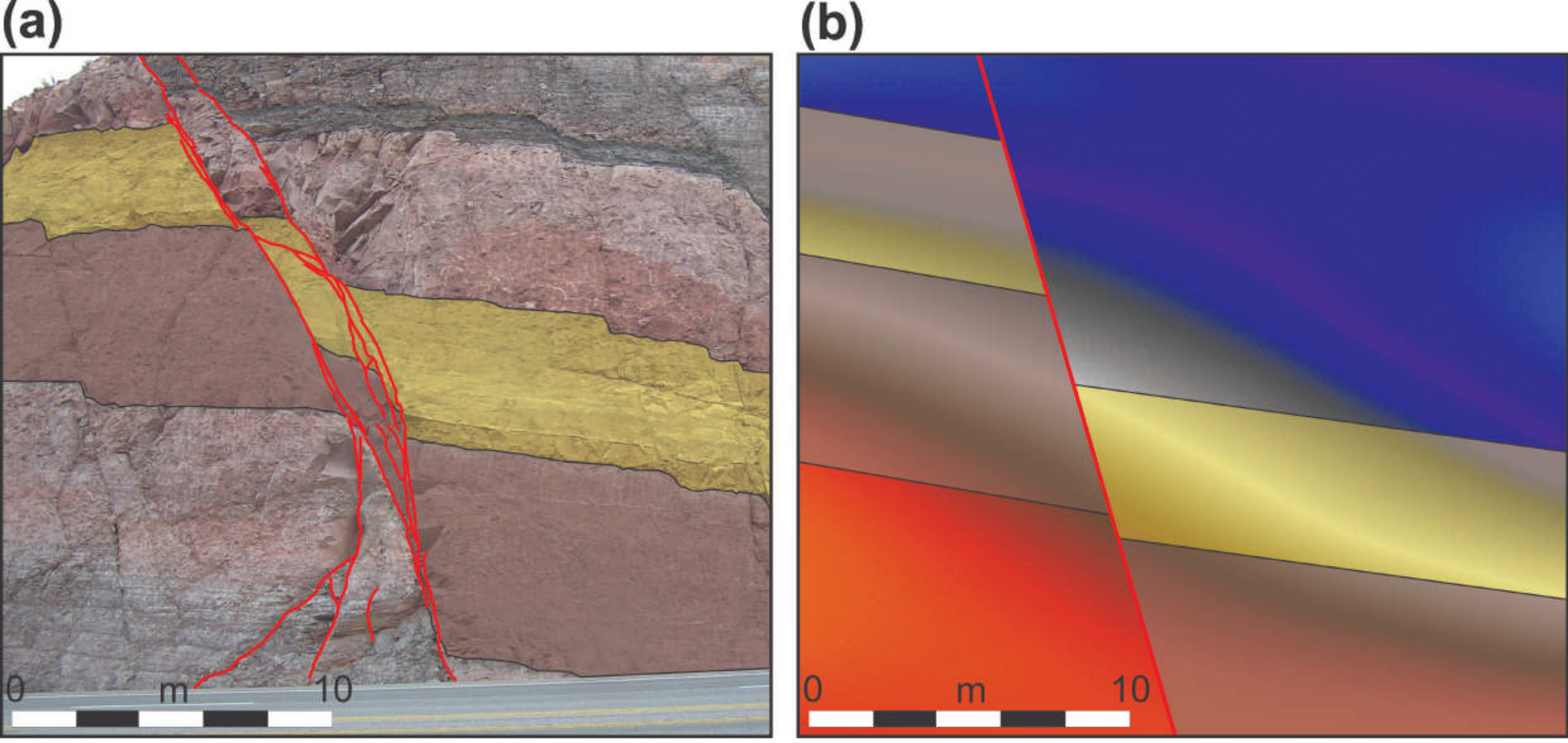
(a)
0
m
10
(b)
0
m
10

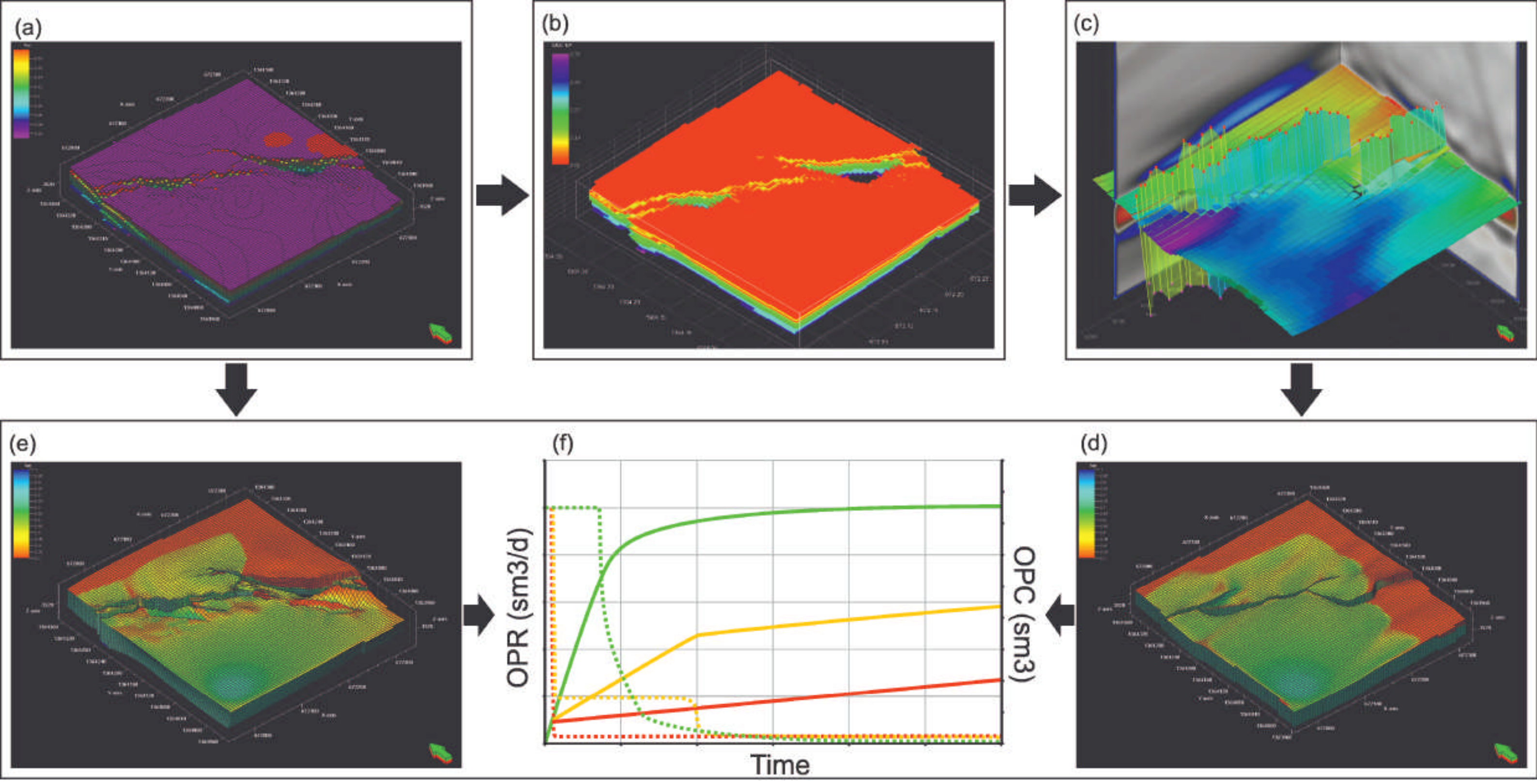
(a)
(b)
(c)
(e)
(f)
(d)
OPR (sm3/d)
OPC (sm3)
Time

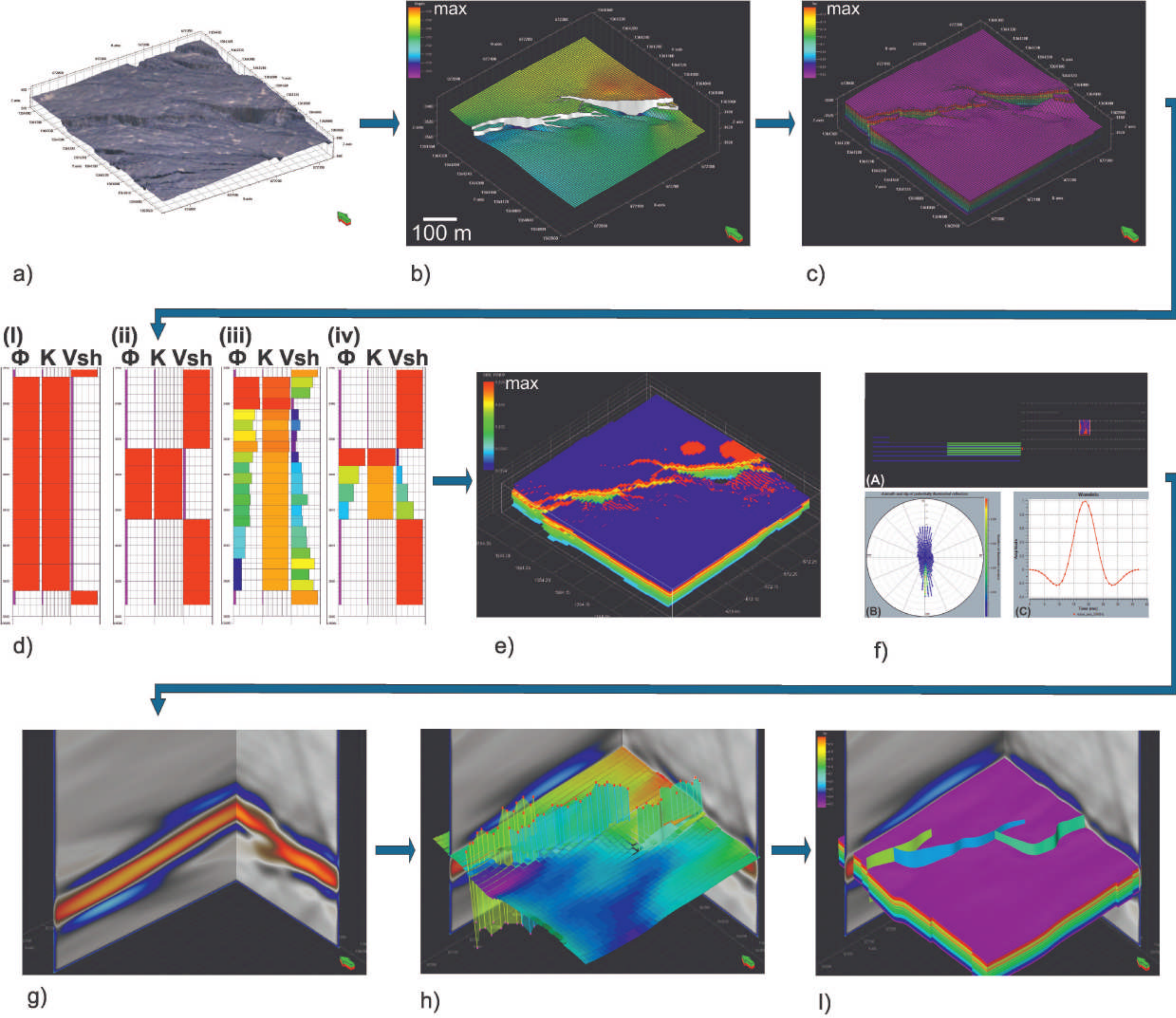

Wood et al., The missing complexity in seismically imaged normal faults: What are the implications for geometry and production response?

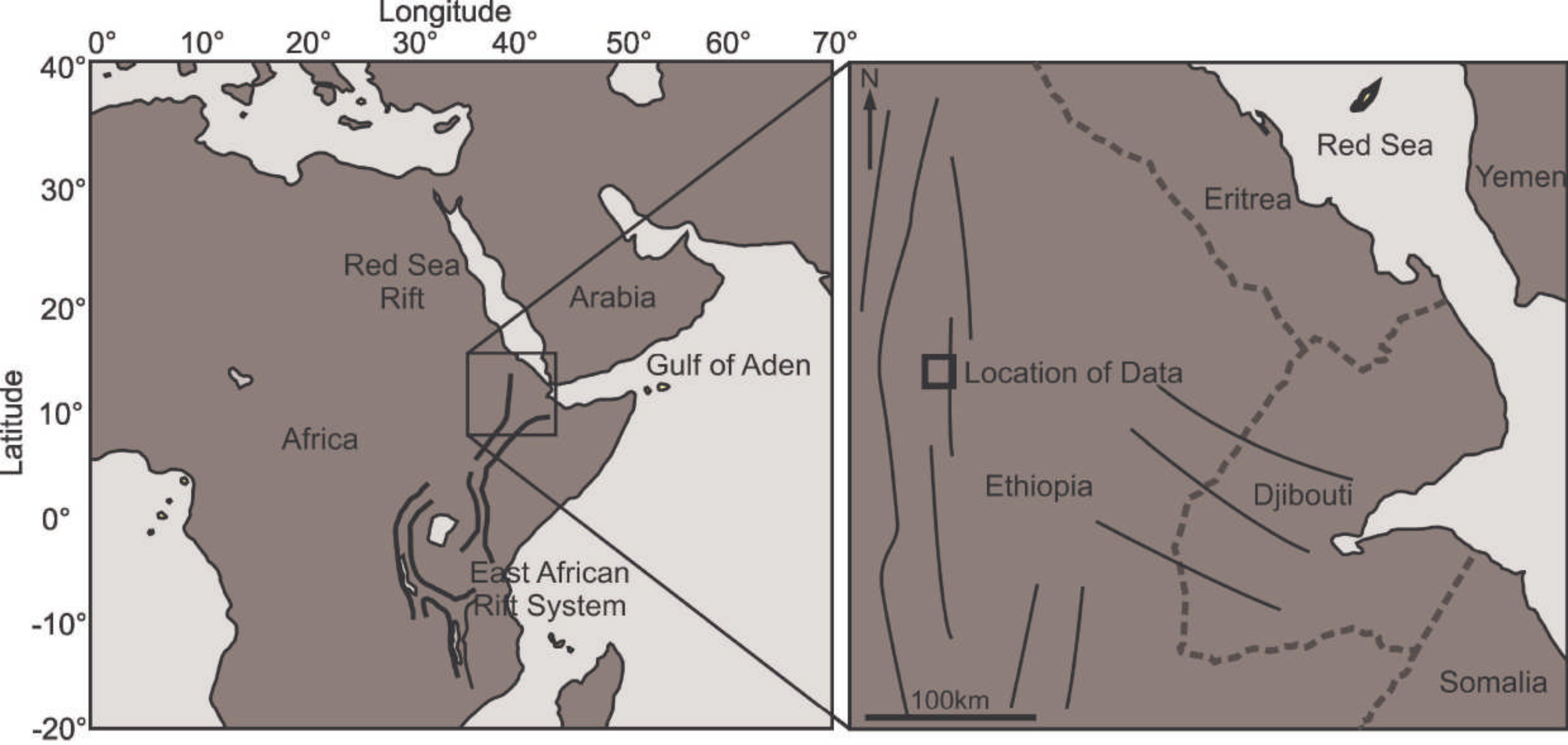
Longitude
0°
10°
20°
30°
40°
50°
60°
70°
40°
30°
20°
10°
0°
-10°
-20°
Latitude
Red Sea Rift
Arabia
Gulf of Aden
Africa
East African Rift System
N
Red Sea
Yemen
Eritrea
Location of Data
Ethiopia
Djibouti
Somalia
100km

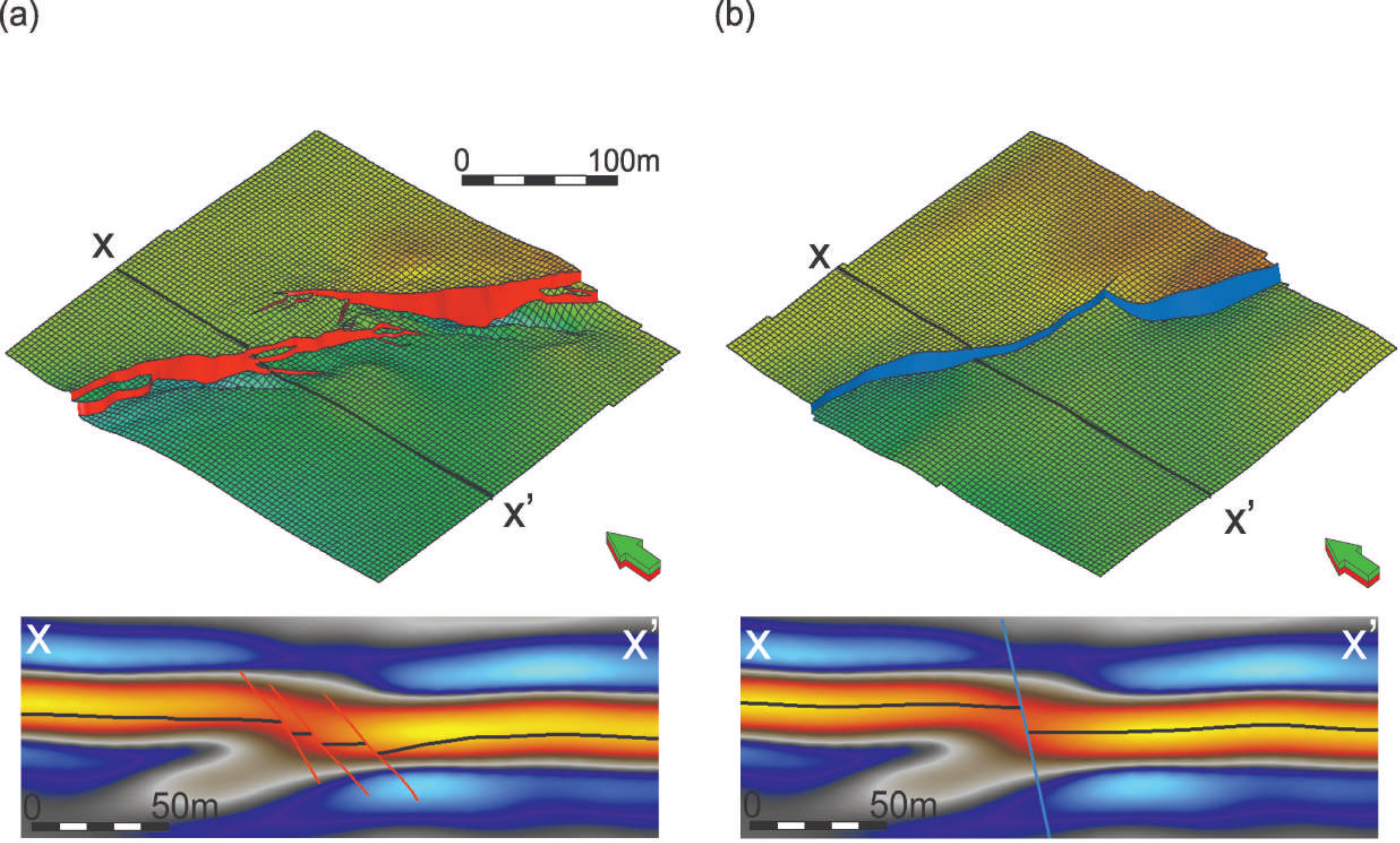
(a)
(b)
0
100m
X
X'
X
X'
0
50m
X
X'
X
X'
0
50m

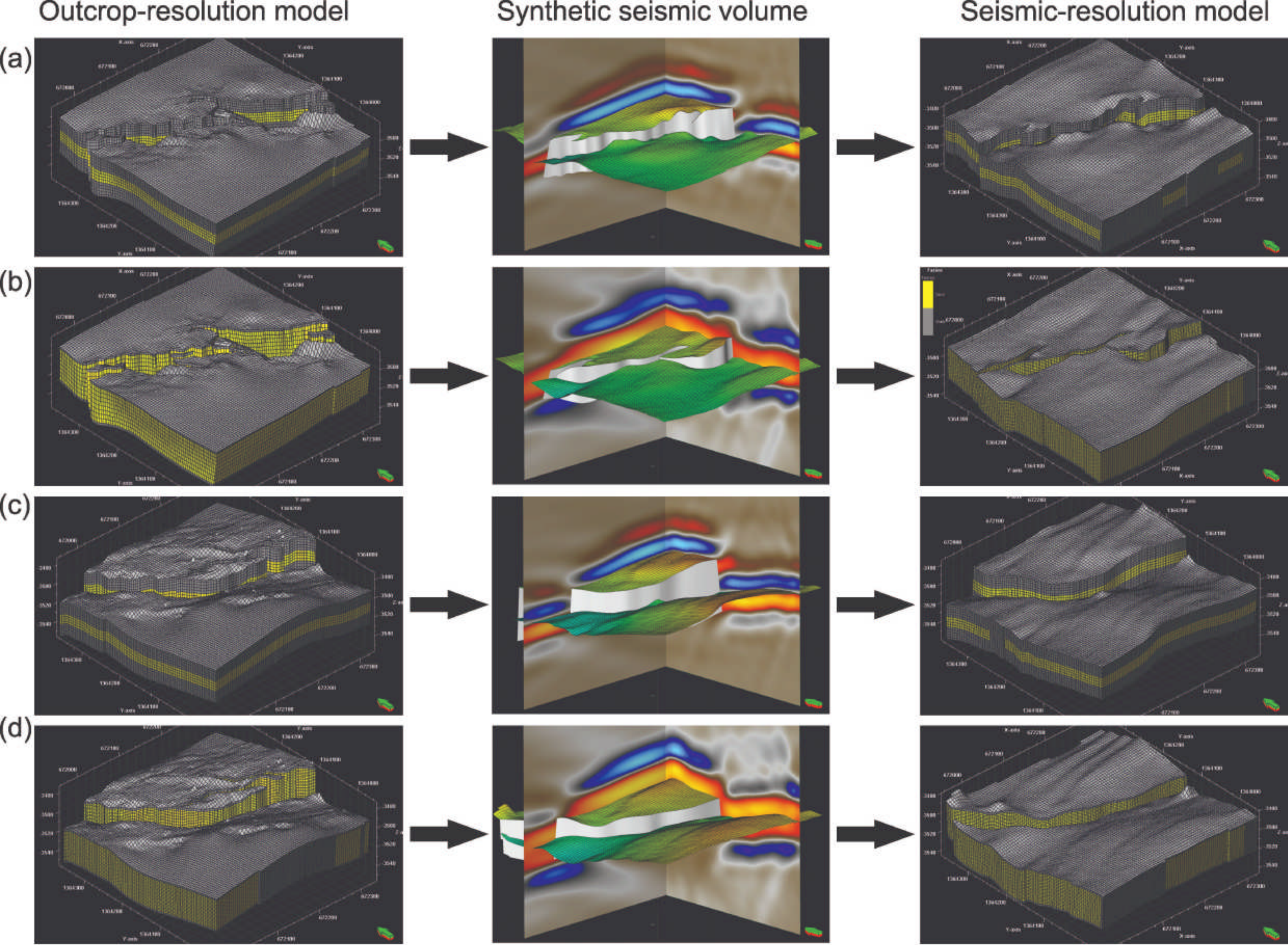
Outcrop-resolution model
Synthetic seismic volume
Seismic-resolution model
(a)
(b)
(c)
(d)

(a) High Th:tw, outcrop: 11000 m^2

(b) High Th:tw, modelled: 5000 m^2

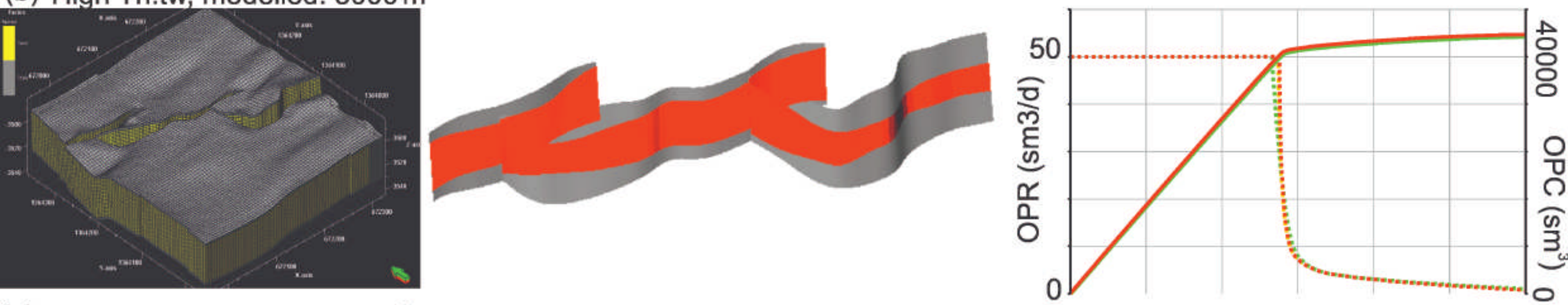

(c) Low Th:tw, outcrop: 1950 m^2

(d) Low Th:tw, modelled110 m^2

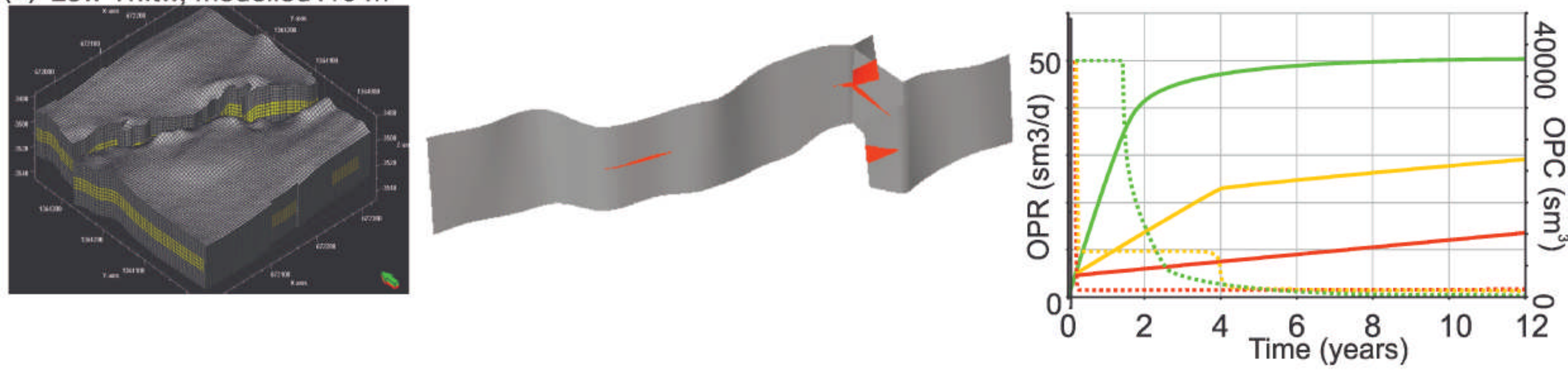

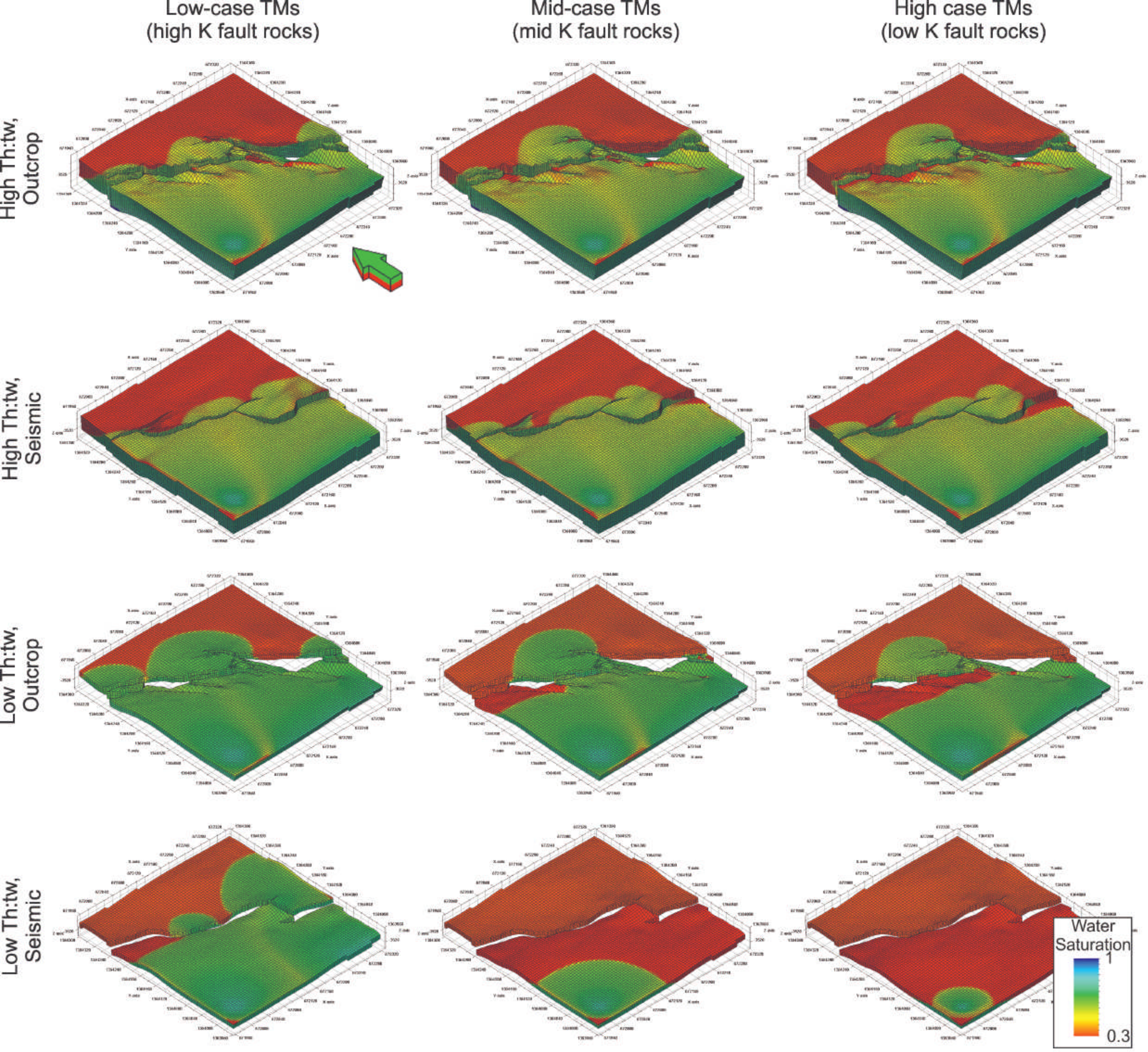
Low-case TMs
(high K fault rocks)
Mid-case TMs
(mid K fault rocks)
High case TMs
(low K fault rocks)
High Th:tw, Outcrop
High Th:tw, Seismic
Low Th:tw, Outcrop
Low Th:tw, Seismic
Water Saturation
1
0.3

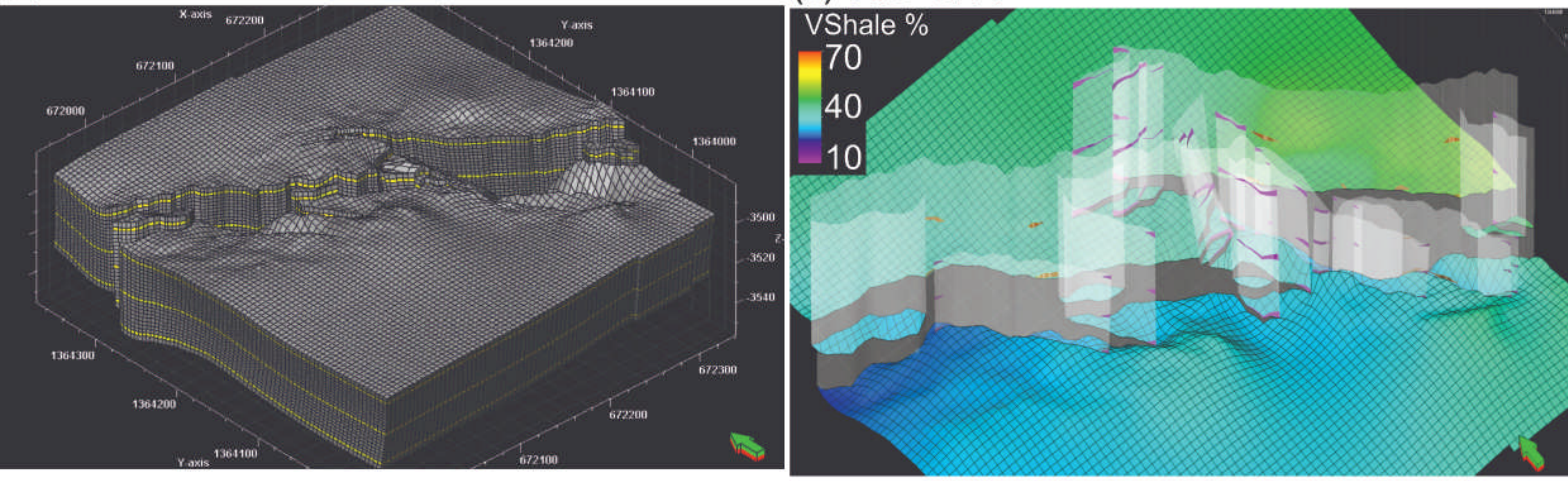

(a) N:G=0.14

(b) N:G=0.14

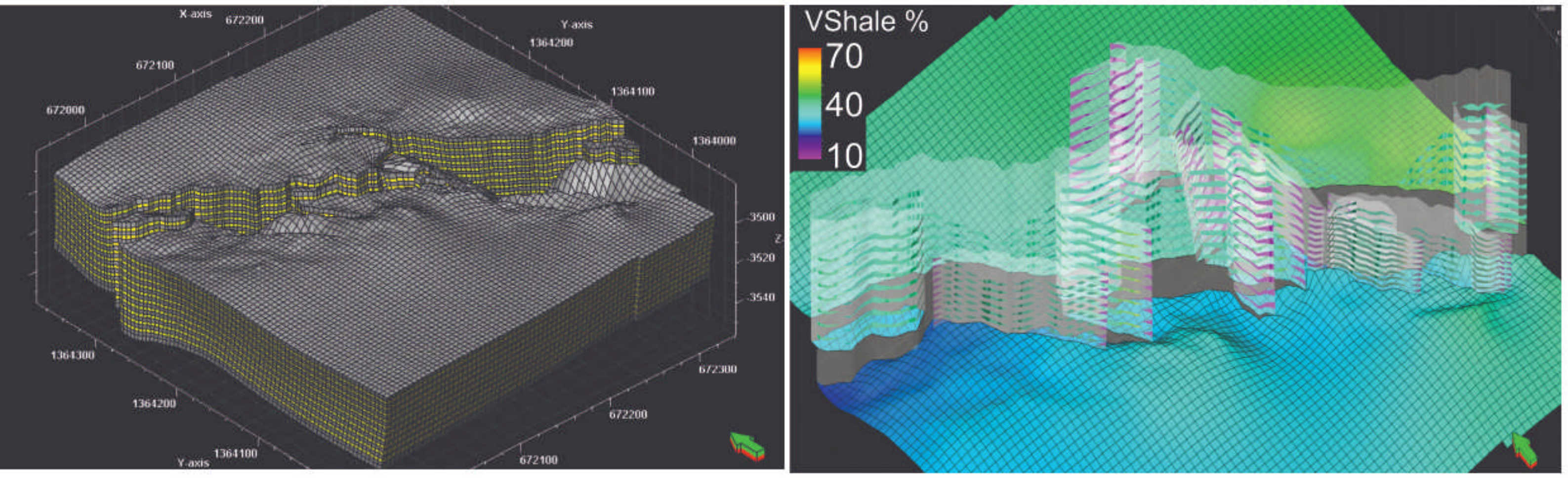

(c) N:G=0.46

(d) N:G=0.46

Figure 10

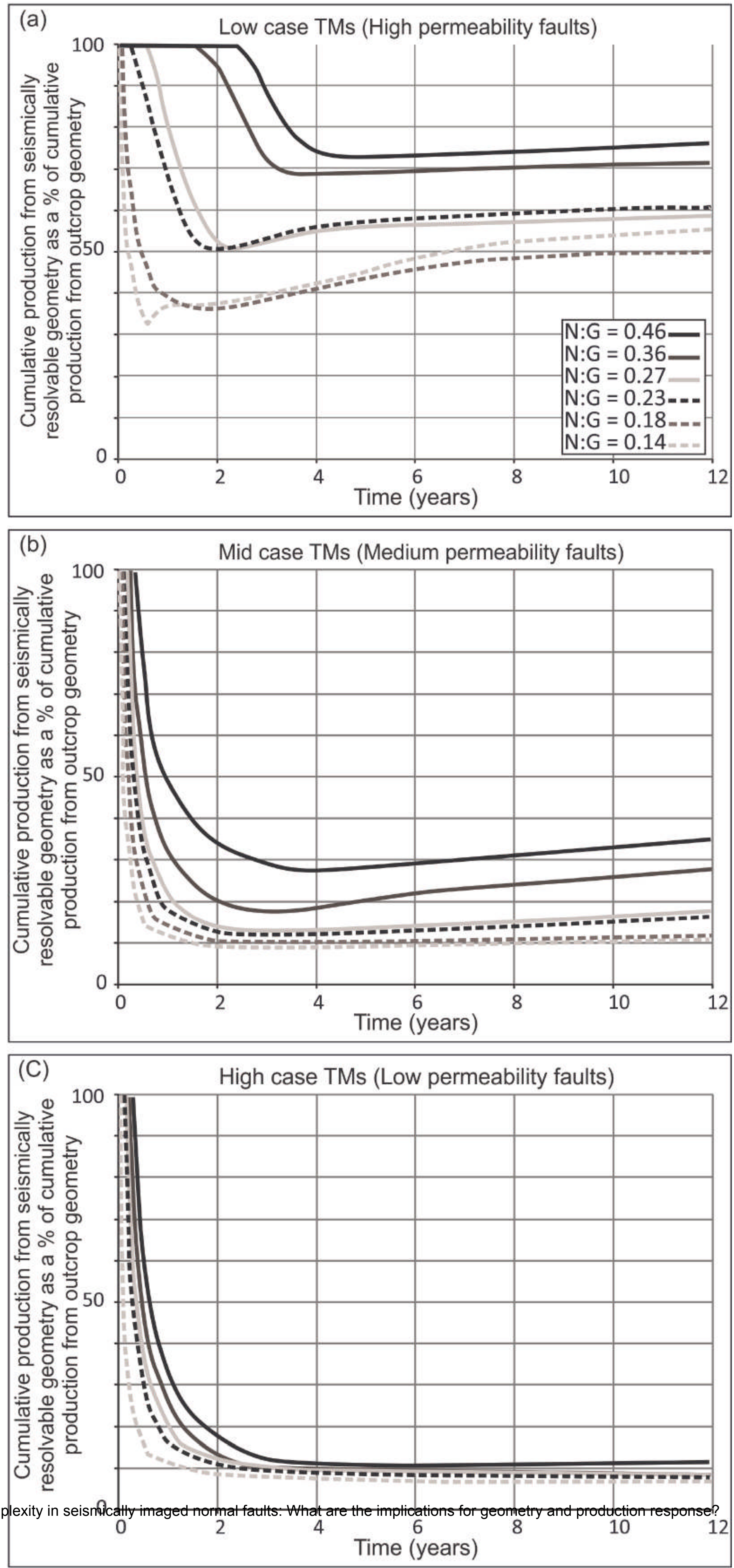
(a)
Low case TMs (High permeability faults)
Cumulative production from seismically resolvable geometry as a % of cumulative production from outcrop geometry
100
50
0
0
2
4
6
8
10
12
Time (years)
N:G = 0.46
N:G = 0.36
N:G = 0.27
N:G = 0.23
N:G = 0.18
N:G = 0.14
(b)
Mid case TMs (Medium permeability faults)
Cumulative production from seismically resolvable geometry as a % of cumulative production from outcrop geometry
100
50
0
0
2
4
6
8
10
12
Time (years)
(C)
High case TMs (Low permeability faults)
Cumulative production from seismically resolvable geometry as a % of cumulative production from outcrop geometry
100
50
0
0
2
4
6
8
10
12
Time (years)

Figure 11

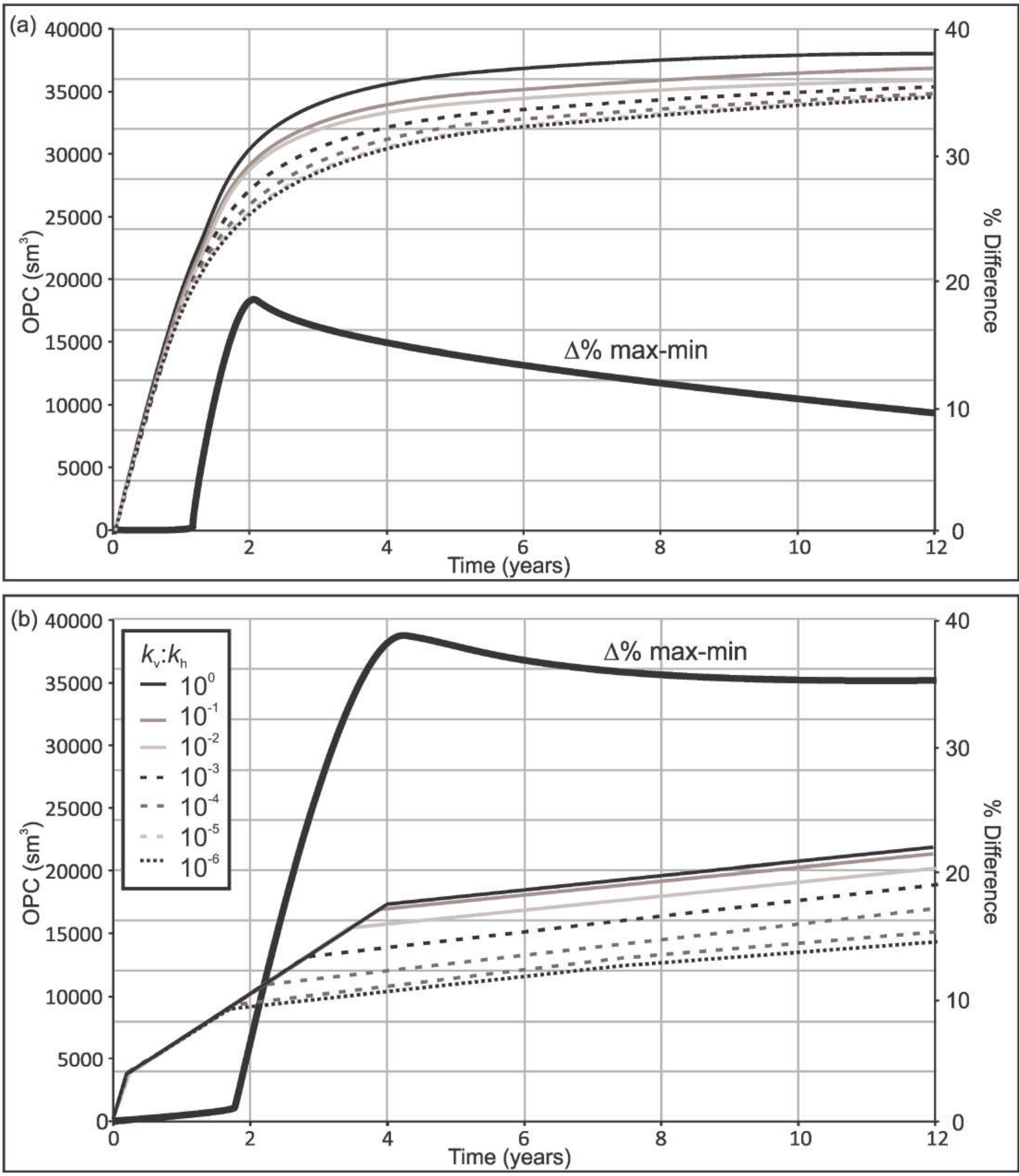
(a)
OPC (sm^3)
0
5000
10000
15000
20000
25000
30000
35000
40000
% Difference
0
10
20
30
40
Time (years)
0
2
4
6
8
10
12
Δ% max-min
(b)
k_v:k_h
10^0
10^{-1}
10^{-2}
10^{-3}
10^{-4}
10^{-5}
10^{-6}
Δ% max-min
OPC (sm^3)
% Difference
Time (years)